

Cite this article as: Xu Hailong, Huang Li, Zhang Wen, et al. Progress of Irradiation-Resistance Materials[J]. Rare Metal Materials and Engineering, 2023, 52(05): 1661-1672.

REVIEW

Progress of Irradiation-Resistance Materials

Xu Hailong^{1,2}, Huang Li², Zhang Wen², Gao Xuanqiao², Yang Yichao^{2,3}, Shan Zhiwei¹, Li Jianfeng²

¹ School of Materials Science and Engineering, Xi'an Jiaotong University, Xi'an 710049, China; ² Northwest Institute for Nonferrous Metal Research, Xi'an 710016, China; ³ Northwestern Polytechnical University, Xi'an 710072, China

Abstract: Developing novel materials for nuclear reactors is a crucial research task. Due to the harsh conditions in the reactors, core materials must possess exceptional high-temperature properties, including high strength, ductility, corrosion resistance, and irradiation resistance. Additionally, the low neutron absorption cross-section and the neutron activation are also important considerations. It is widely acknowledged that the choice of core material for a typical space nuclear reactor is primarily determined by the operation temperature. Generally, with increasing the designed operation temperature of reactor, 316 stainless steel, nickel-based superalloys, oxide-dispersion-strengthened (ODS) steel, refractory metals, and SiC ceramics are preferred in order. Besides, the high entropy alloys attract extensive attention for nuclear applications. This review summarizes the evolution of mechanical properties of different material systems during irradiation process, providing guidance for the further research in irradiation resistance.

Key words: irradiation resistance; mechanical properties; nuclear engineering

With the increasingly fierce international competition, deep space exploration becomes important strategic technology, which is closely related to the exploration and application of future space resources. Similar to most core technologies, the continuous and stable supply of energy and power is a crucial challenge for deep space exploration. Under complex space environments, traditional nuclear power sources, such as chemical fuels and solar batteries, have severe challenges. Due to the high temperature, severe corrosion, and high doses of ion bombardment in nuclear reactors during service^[1], materials with good irradiation resistance are characterized by high melting point, low neutron absorption cross-section, and low sputtering yield^[2]. The latter two characteristics are the vital bases for the material to maintain the structural stability in the interaction with neutrons.

The core material of a typical space nuclear reactor is mainly determined by the operation temperature^[3]. When the designed operation temperature of reactor is less than 900 K, 316 stainless steel is the preference^[4]. When the designed operation temperature of reactor is 1000–1200 K, the nickel-based superalloys, such as Inconel-601^[5] and Hastelloy-X^[6] alloys, are preferred. Oxide-dispersion-strengthened (ODS) steel^[7] and niobium alloy^[8] are more suitable when the

operation temperature is 1200–1500 K. When the operation temperature exceeds 1500 K, the refractory metals, such as titanium-zirconium-molybdenum alloys, molybdenum-rhenium alloys, and tungsten-rhenium alloys, attract much attention^[9]. SiC ceramics are more suitable in higher temperature environments. Additionally, the high entropy alloys (HEAs) possess high structural stability and excellent mechanical properties under irradiation environment, which attract much attention in the nuclear field^[10].

1 Stainless Steel

AISI 304 and 316 austenitic stainless steels have optimal combination of strength, ductility, and corrosion resistance. Huang et al^[11] proposed a deformation mode map of irradiated 316 stainless steels in true stress-dose space for tensile tests at room temperature, as shown in Fig.1^[12]. It can be seen that the true stress for formation of extended stacking fault, twinning, and plastic instability (necking) is dose-independent, and thus it can be measured at un-irradiated state. With the dose of a little displacement per atom (dpa), the yield stress reaches the necking stress, namely PIS, and the uniform elongation is quasi-null^[11–12]. The effect of tensile temperature on the plasticity mechanisms after irradiation has been researched^[13].

Received date: October 08, 2022

Corresponding author: Xu Hailong, Master, Senior Engineer, Northwest Institute for Nonferrous Metal Research, Xi'an 710016, P. R. China, Tel: 0086-29-86231105, E-mail: 187298751@qq.com

Copyright © 2023, Northwest Institute for Nonferrous Metal Research. Published by Science Press. All rights reserved.

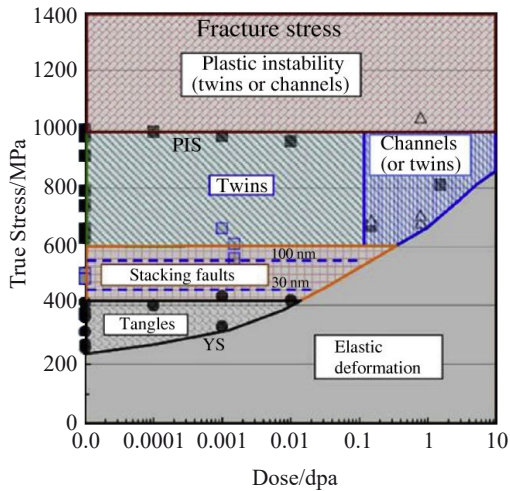


Fig.1 Deformation mode map of 316 and 316LN stainless steels in true stress-dose space^[12] (PIS: plastic instability stress, onset of necking; YS: yield stress; dpa: displacement per atom)

When the tensile temperature varies from $-115\text{ }^{\circ}\text{C}$ to $120\text{ }^{\circ}\text{C}$, $\gamma \rightarrow \alpha$ transformation occurs in the austenitic steels, resulting in the recapture ductility. Although the dose threshold of wave initiation of the irradiated alloy at room temperature can hardly be reached, the wave generation can be induced with decreasing the tensile temperature^[13]. The formation of twins and martensite laths after irradiation has been extensively studied during tension at temperature higher than $300\text{ }^{\circ}\text{C}$.

Austenitic steels with excellent high-temperature strength attract much attention as the structural materials of fusion reactors. However, the austenitic steel has many deficiencies, such as low thermal conductivity, weak radiation resistance, inferior swelling performance, low activation requirements, and low yield strength, which need to be improved by process optimization or addition of specific elements.

Thus, a series of modified cast stainless steels based on the standard 316L alloy have been developed and characterized. The steels are modified by addition of nitrogen, manganese, and copper to improve their mechanical performance under both irradiated and un-irradiated conditions^[14–15]. The modified cast steels exhibit less elemental inhomogeneity and secondary phase formation, compared with the steels before modification. The ferrite formation during casting and the subsequent precipitation during ferrite reversion process are effectively suppressed in the modified steels^[16].

The reduced activation ferritic/martensitic (RAFM) steel is usually used as the wall/cladding structural material for the fusion engineering testing reactors^[17], including the EURO97 steel, F82H steel, JRF-1 steel, and 9Cr2WVTa steel^[18–19]. The ultra-clean reduced activation martensitic steel can be prepared by ultra-clean process preparation technology^[20], involving the vacuum induction melting combined with protective atmosphere electroslag remelting duplex process, to replace Ta element with the less active Ti element. The prepared steel exhibits extremely strong precipitation phase, good ductile-brittle transition temperature stability, and fine

irradiation resistance.

RAFM steel has better performance than the austenitic stainless steel in the application of structural materials for fusion reactor. RAFM steel has mature manufacturing process, good weldability, fine radiation swelling resistance, fine thermal stress factor, excellent corrosion resistance against liquid metals, and available irradiation properties^[21]. The improved Fe-Cr-Mo RAFM steel has been widely researched and found that the Mo, Ni, and Nb elements in the original RAFM steel cannot meet the requirements of low activation, which should be replaced by W, Ta, and V elements^[22].

The deuterium retention in RAFMs, castable nanostructured alloys (CNAs), and ODS steels for the fusion reactor application is widely studied. D^+ implantation at room temperature and 10 keV followed by thermal desorption spectroscopy (TDS) can quantitatively measure the deuterium retention. ODS steels have the largest deuterium retention (sink strength) among various materials, which is almost one order of magnitude higher than that of pure iron, 6 times higher than that of RAFM, and 2–4 times higher than that of CNA steels, as shown in Fig.2^[23]. Most implanted deuterium is desorbed when temperature is lower than 600 K, implying that these trapping sites are weak. Additionally, the differences in nanoparticles and grain/lath boundaries are primarily responsible for the differences in deuterium retention, while other trapping sites (vacancy clusters, dislocations) have relatively less contribution. The deuterium retention is not linearly correlated to the sink strength of the materials. It is concluded that the complicated nanostructures lead to the enhanced deuterium retention of advanced steels for the fusion reactor application.

Neither the mechanism of irradiation-induced damage in stainless steels nor the interplay among the damage, clear bands, twinning, and martensite formation is clear. Particularly, the facts that the critical stresses for twinning, formation of extended stacking fault, and necking are dose-independent, whereas the microstructural evolution is dose-dependent

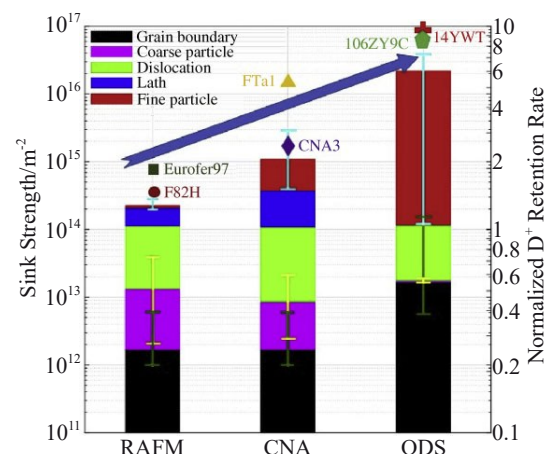


Fig.2 Sink strength and normalized deuterium retention rate of RAFM, CNA, ODS steels (normalized to the desorbed deuterium from pure iron)^[23]

should also be investigated. The grain rotation in irradiated steels during tensile tests should also be studied.

2 Ni-based Superalloys

Commercial Ni-based superalloys are commonly considered for nuclear applications due to their excellent mechanical properties and fine corrosion resistance at specific reactor temperatures. Among those commercial Ni-based alloys, Inconel 718 alloy possesses improved age-hardening capability and comparable corrosion resistance, which can be used as core components in light water reactors^[24]. With increasing the radiation dose, the alloy ductility is increased. A solution-annealed Inconel 718 alloy irradiated to approximately 9 dpa has the yield strength of around 1 GPa and elongation of approximately 19%^[24]. It is also found that both the uniform and total elongation values are increased with increasing the radiation dose from 2.5 dpa to 9.7 dpa, as shown in Fig.3^[24]. According to Ref.[24], the high-resolution transmission electron microscopy (TEM) and energy dispersive spectroscopy were conducted at atomic resolution level. The stacking faults and vacancy clusters of nanometer scale associated with H and He can be observed. These radiation-induced defect structures may increase the strain-hardening effect on material during deformation. Besides, the ductility is increased with increasing the dose. The mechanical performance of Inconel 718 alloy after irradiation to 9.7 dpa is favorable, providing support to prolong the proton beam window service lifetime with higher displacement dose levels. After irradiation to approximately 9.7 dpa, the strength

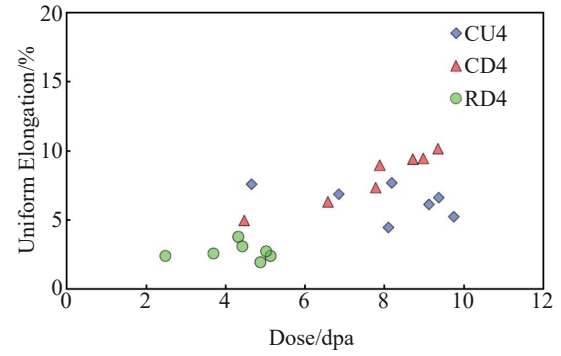


Fig.3 Relationship between uniform elongation and dose^[24]

remains, but the ductility decreases, which agrees with results of irradiated SA 718 alloy^[25].

The 625 Plus alloy is a commercial Ni-based alloy as promising structural material for nuclear reactors. The long-term thermal aging was conducted to clarify the microstructure evolution of 625 Plus alloy under proton and ion irradiation at 300 °C, as shown in Fig.4^[26]. The <100> zone of 625 Plus alloy was analyzed by selected area electron diffraction (SAED) through TEM. Atom probe tomography (APT) was also conducted for element distribution analyses. Cascade mixing dominates during ion irradiation. The comparison between alloys after solution and aging treatments reveals the steady pattern of the secondary phase at nanoscale. The phase separation, formation of Pt₂Mo-type ordered phase and γ' phase, and solute clustering of Nb, Ti, Al, and Si all

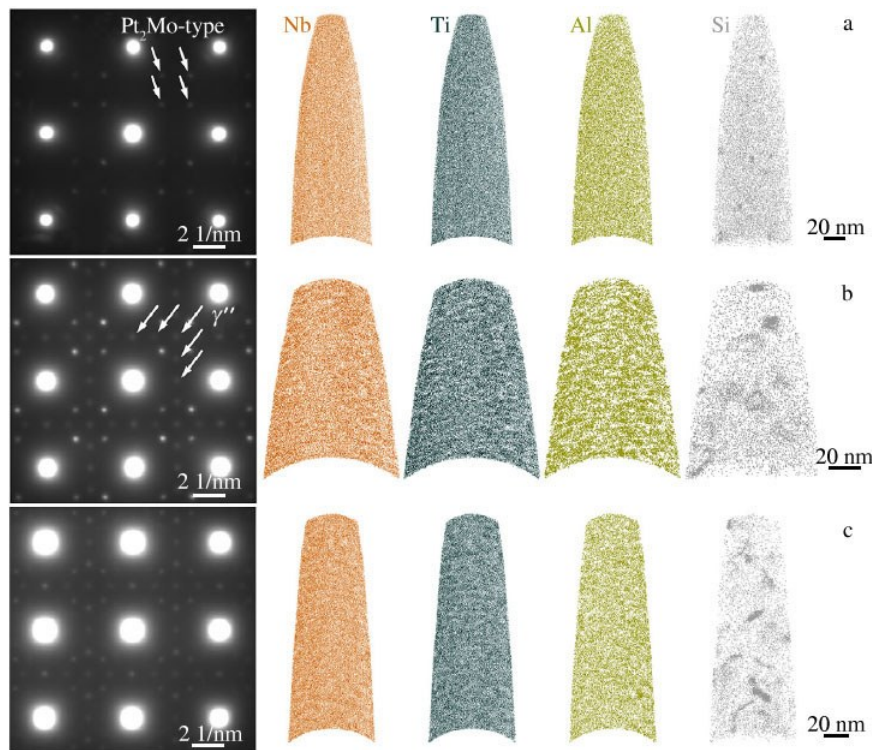


Fig.4 SAED patterns and APT element distribution results of <001> zone of 625 Plus alloy after proton irradiation to 1.5 dpa (a), 6 dpa (b), and 11 dpa (c) at 300 °C^[26]

occur in the solution-treated alloys after proton irradiation at 300 °C. With dose of 1.5–11 dpa, the presence of Pt₂Mo-type ordered phase can be clearly observed. With dose of 6 and 11 dpa, the superlattice spots of γ phase can also be observed. The Nb-rich clusters are uniformly distributed. Thus, the Al-rich and Nb-rich clusters are precursors of Ni₃(Ti, Al, Nb) γ' phase and Ni₃(Nb, Mo, Ti, Al) γ'' phase precipitates, respectively. Si-rich clusters can be observed with dose of 1.5–11 dpa.

3 Refractory Alloys

Tungsten, niobium, molybdenum, and other refractory metals have high melting points and low sputtering yields. Therefore, the development of anti-irradiation materials attract much attention.

3.1 Nb alloys

Niobium and its alloys are promising structural materials for compact nuclear reactors at high temperature due to their good ductility, high temperature strength, fine corrosion resistance against most liquid metals or coolants, and low density^[27].

Nemoto et al^[28] studied the mechanism of ultra-high irradiation hardening on Nb by in-situ uniaxial tension and compression tests. He bubbles in Nb promote the dislocation nucleation. In addition, He bubbles with 1.2 nm in size jointly form a multi-sided fracture surface, whereas those with 8.0 nm in size cause material failure due to elongation and fragmentation. The theoretical hardening value is less than the one-third of the experimental result. The huge difference in theoretical and experimental results is caused by the ultra-high irradiation hardening originating from a large number undetectable He-vacancy (He-V) complexes with atom size. The strong interactions between dislocations and high-density He-V complexes result in the significant irradiation hardening in Nb.

The high-temperature strength of pure Nb decreases above 1000 °C. The addition of Zr and C into Nb is an effective method to enhance the material strength. Nb-1Zr-0.1C alloy is also a promising structural material for compact nuclear reactor at high temperature^[29]. The defect structure evolves within the grains after irradiation to the highest dose of 1×10^{18} particle/cm², as shown in Fig. 5. The planar defects, such as dislocation loops, can be clearly observed. The size of the dislocation loops is 3–10 nm, and the average dislocation loop size is approximately 6 nm. Dislocation loops result from the collapse of irradiation-induced defect clusters.

The relationship between engineering stress and plastic strain of un-irradiated and irradiated Nb-1Zr-0.1C alloys is shown in Fig. 6^[29]. It is apparent that the proton irradiation has significant effect on the mechanical behavior of Nb-1Zr-0.1C alloy. The yield strength and ultimate tensile strength of the alloy are increased, whereas the ductility (uniform and total elongation) is reduced after irradiation. Correspondingly, the ultimate compressive strain ε_c and the ultimate tensile strain ε_t of the un-irradiated alloy decreases from 5.00 and 9.7% to

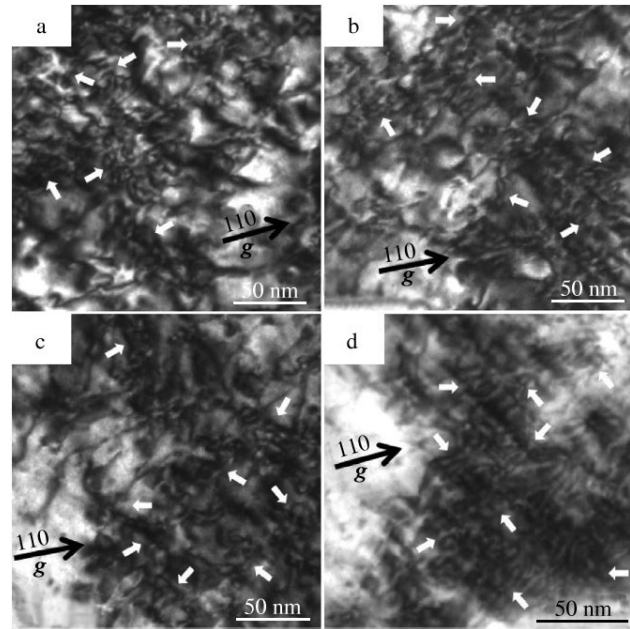


Fig. 5 Bright-field (BF) TEM microstructures (the defect structure evolves) of Nb-1Zr-0.1C alloy after irradiation to dose of 1×10^{18} particle/cm² (dislocation loops are marked by arrows)^[29]

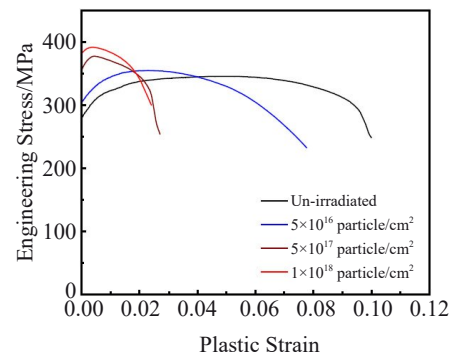


Fig. 6 Relationship between engineering stress and plastic strain for un-irradiated and irradiated Nb-1Zr-0.1C alloys^[29]

0.34 and 1.8% when the dose is 1×10^{18} particle/cm², respectively. This result infers the occurrence of irradiation embrittlement in the Nb-1Zr-0.1C alloy.

3.2 Mo alloys

Molybdenum has a body-centered cubic (bcc) crystal structure. No phase change occurs during the heating process to melting point, which indicates the excellent high-temperature structural stability and superior high-temperature performance of molybdenum alloys^[30]. However, the mechanical properties of metals with bcc structure at room temperature are inferior, such as low plastic deformation ability and weak process hardening ability^[31], even for the industrial-pure Mo.

The evolution of dislocation rings and the interaction of pre-existing dislocation lines in molybdenum under He⁺ irradiation at 673 K and 30 keV were analyzed through in-situ TEM and molecular dynamics simulations^[32-33]. It is found that

with increasing the helium dose, the density of dislocation ring is increased rapidly and then slowly decreased to the saturation value, whereas the average size of dislocation ring is continuously increased until the upper limit. Pre-existing dislocation lines inhibit the nucleation and growth of dislocation rings, and the irradiation-induced dislocation rings have a strong pegging effect on the dislocation lines, thereby hindering the dislocation movement. As shown in Fig.7, both $1/2\langle 111 \rangle$ and $\langle 100 \rangle$ loops are formed with the proportion of 60.2% and 39.8% at $3.95 \times 10^{15} \text{ He}^+/\text{cm}^2$ (0.07 dpa), respectively^[33]. The interaction process depends on the Burgers vector, the plane of dislocation loop, the motion and reaction kinetics of dislocation segments, and the external loading. The simulated and experimental results of these phenomena are in great agreement.

Since 1960, the molybdenum-rhenium alloy has become the most commonly used core structural material^[34]. The addition of Re element can greatly improve the high-temperature strength, processing performance, welding performance, and recrystallization temperature of solid-solution-strengthened molybdenum alloy, and significantly reduce the toughness

transition temperature and anisotropy of molybdenum alloy, thereby significantly improving the room-temperature mechanical properties of molybdenum alloy. In addition, molybdenum-rhenium alloy has good compatibility with nuclear fuels, such as UO_2 , UN, UC, and alkali metals in heat transfer media. Therefore, molybdenum-rhenium alloys attract much attention as core materials for high-temperature heat pipe reactor^[35].

The molybdenum-rhenium alloy can be roughly divided into low rhenium alloy (rhenium content of 2wt%–15wt%), medium rhenium alloy (rhenium content of 15wt%–30wt%), and high rhenium alloy (rhenium content of 30wt%–50wt%)^[36]. The irradiation damage degree of molybdenum rhenium alloys is affected by the irradiation temperature and the rhenium content in the alloy^[37]. Agarwal et al^[38] studied the irradiation damage, recrystallization, and stress release of Mo-2Re, Mo-4Re, Mo-10Re, Mo-13Re, Mo-41Re, and Mo-41Re molybdenum-rhenium alloys at 681 – 1072 K. When the irradiation temperature is less than 874 K, the hardness of molybdenum-rhenium alloy after irradiation is increased linearly with increasing the rhenium content. At the irradiation

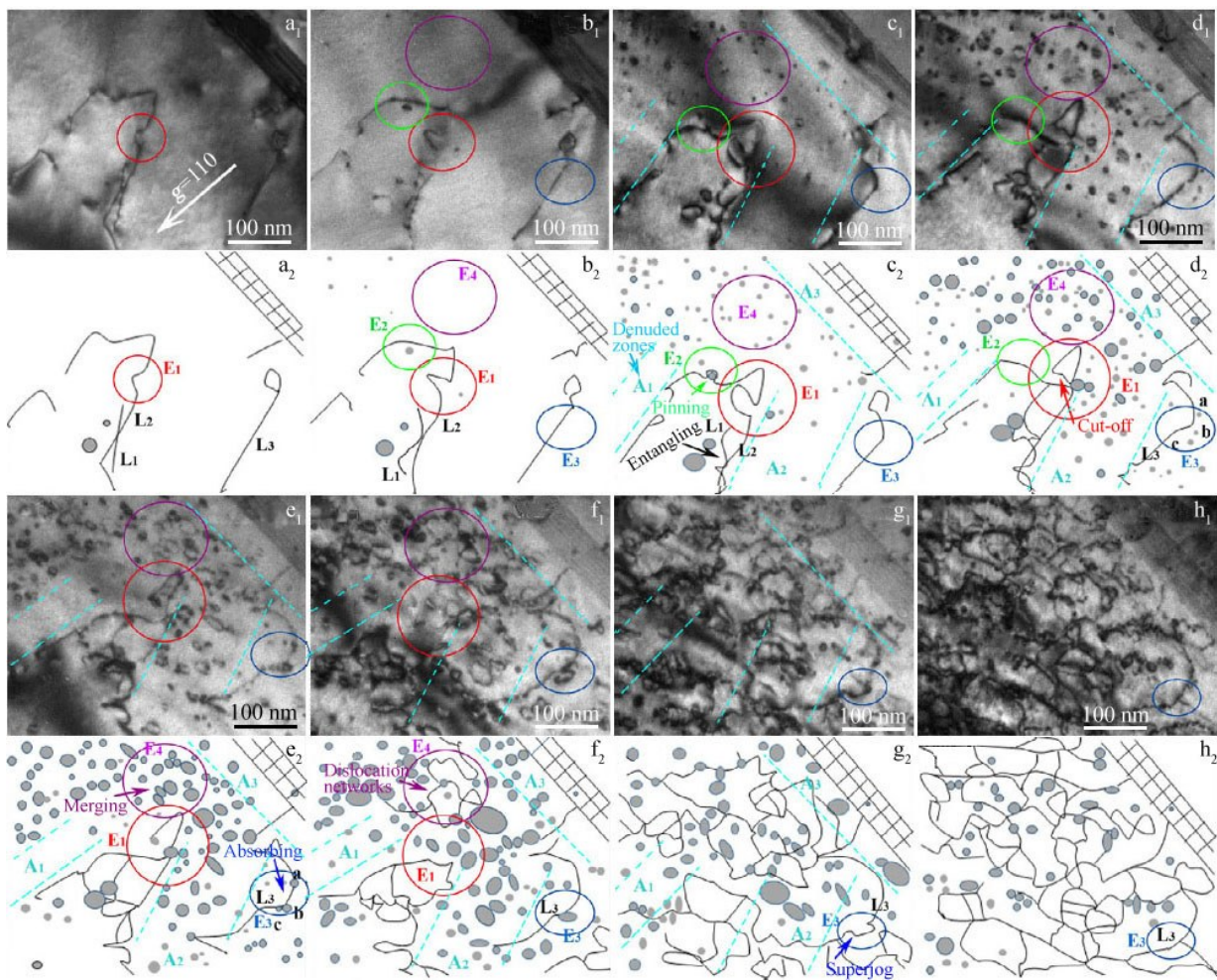


Fig.7 Experimental (a₁-h₁) and simulated (a₂-h₂) evolutions of dislocation loops and pre-existing dislocation lines before (a₁-a₂) and after He⁺ irradiation with dose of 0.02 dpa (b₁-b₂), 0.04 dpa (c₁-c₂), 0.07 dpa (d₁-d₂), 0.11 dpa (e₁-e₂), 0.14 dpa (f₁-f₂), 0.21 dpa (g₁-g₂), and 0.28 dpa (h₁-h₂)^[33]

temperature of 1072 K, although the increase in hardness is not that obvious with increasing the rhenium content, the maximum hardness of the molybdenum-rhenium alloy after irradiation is still twice larger than that of the alloy before irradiation. The severe irradiation hardening of molybdenum-rhenium alloys at irradiation temperatures less than 1000 K reflects a significant decrease in plasticity of molybdenum-rhenium alloys at low irradiation temperatures accompanied by more severe grain boundary fractures^[39-40], as shown in Fig.8.

The evolution of dislocation rings in raw and nanocrystalline Mo-5wt% Re alloys during irradiation was analyzed by in-situ TEM characterization^[41]. Cyclic activation of dislocation rings can be observed during Fe⁺ irradiation at 700 and 800 °C and 400 keV. The gradual disappearance of dislocation lines towards the grain boundaries and the change of the slip surface from [101] to [211] can be observed after in-situ irradiation. There are three main pathways leading to the disappearance of dislocation ring: the aggregation between dislocation rings, the absorption of strong defects, and the influence of surrounding dislocation rings. With increasing the irradiation dose, the number of dislocation rings formed in the coarse grains is gradually increased, the density of dislocation lines is almost stable, whereas the number of dislocation rings

produced in the nanocrystals is relatively small.

3.3 W alloys

As a typical refractory metal with high melting point and low sputtering yield, tungsten is favored for plasma-facing materials (PFMs) in fusion devices under extreme conditions^[42], and its behavior under irradiation and He plasma interaction has been extensively studied. He ion-beam irradiation damage effects on the mirror-polished single-crystalline W samples with {100}, {110} and {111} surface planes were discussed in Ref. [43]. Irradiation was performed at room temperature and 40 keV with He⁺ dose of 1×10^{16} particle/cm² followed by TDS to approximately 1920 K. The microstructures of He-irradiated W alloy before and after TDS treatment were characterized by scanning electron microscope (SEM) coupled with transmission kikuchi diffraction (TKD) technique and TEM, as shown in Fig. 9^[43]. Corresponding inverse pole figures (IPFs) are also presented in Fig. 9. The He bubbles on subsurface can be observed in all specimens. However, newly formed <111>-oriented surface grains and surface blisters can only be observed along W {100} and W {110} orientations. These results reveal that the radiation damage, He thermal desorption, and surface/subsurface evolution are all strongly dependent on the crystallographic orientation. Related physical mechanisms are discussed based on the ion channeling effects, He-vacancy interactions, and surface diffusion.

The appearance of intermetallic Re precipitation with concentration below the solubility limit is an obscure phenomenon in neutron-irradiated W alloys. Ion irradiation cannot produce intermetallic Re precipitation, indicating that the neutron damage, microstructure evolution, and precipitate formation can hardly be explained. Senkov et al^[44] induced the WRe and WRe₃ phases into W26Re alloy after Ne ion irradiation at 350 keV and 500/800 °C. The precipitation of these phases is related to the effects of cascade energy density and ballistic mixing during high-energy self-ion irradiations, resulting in the re-dissolution of precipitates. Fig.10 shows the BF-TEM images of W26Re alloys before and after irradiation. Single-phase crystallinity is confirmed by SAED patterns along [113] zone axis. After irradiation at 800 °C to 5.0 dpa,

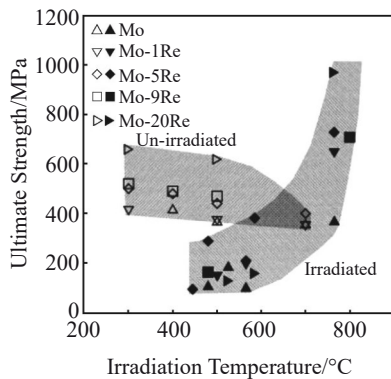


Fig.8 Relationship between tensile strength and irradiation temperature of Mo-Re alloys^[40]

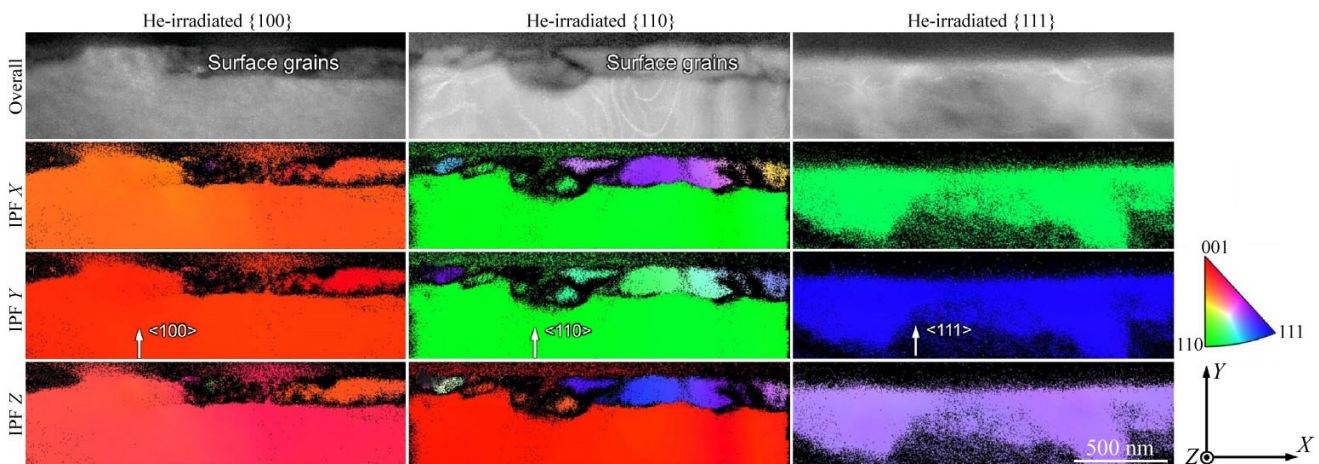


Fig.9 SEM-TKD morphologies of different surface planes of He-irradiated thin foils of W alloys^[43]

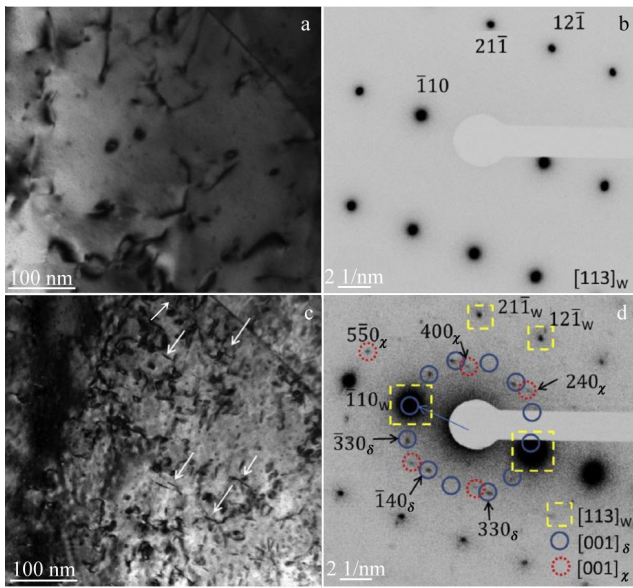


Fig.10 BF-TEM images (a, c) and SAED patterns (b, d) of single-phase crystal for W26Re alloys before (a–b) and after (c–d) Ne ion irradiation at 350 keV and 800 °C with dose of 5.0 dpa (precipitates are indicated by arrows)^[44]

the precipitates nucleate epitaxially, reflecting the relationship between the matrix and precipitates.

The microstructure in W(Re, Ta) alloys exhibits a higher dislocation ring density, compared with that in pure W. The dislocation is increased sharply towards the damage saturation with increasing the dose. Chen et al^[45] performed the high-temperature annealing of pure tungsten followed by irradiation of W ions at 500–1200 °C. At temperatures of 800, 950, 1100, and 1400 °C, the pure tungsten after ion irradiation (2 MeV W⁺, 500 °C, 1014 W⁺/cm²) was subjected to batch isothermal annealing for 0.5–8 h. The dislocation rings with diameter greater than 2–3 nm have the Bertrand vectors of 1/2 <111> and gap properties.

Dobbelstein et al^[46] performed the in-situ W⁺ ion irradiation at 150 keV on W-5wt% (Re, Ta, V) alloys, and studied the effects of irradiation temperature, dose, alloying elements, and grain orientation on the radiation damage and microstructure evolution. For irradiation at 30–1073 K, the defect in pure W

firstly appears at doses ≤ 0.01 dpa as a vacancy ring with Bursell vector of $b=1/2\langle 111 \rangle$. With increasing the irradiation temperature, the number of retained defects is increased sharply, and the maximum cluster size is increased from 1300 dot defects at 30 K to 2300 dot defects at 1073 K. The evolution of damage microstructures at all irradiation temperatures involves the defect cluster migration with varying the dose from 0.1 dpa to 1.0 dpa. The mutual elastic interactions occur during irradiation, leading to the spatial inhomogeneities and loop reactions.

The loop defect size distributions of different W alloys after irradiation to 1.0 dpa are shown in Fig.11^[47]. In pure W alloy, the loop size is increased with increasing the irradiation temperature. At 773 K, small loops with size of 4 nm dominate; at 873 K, the loops with size of 4–5 nm dominate; at 1073 K, the loops with size of 5–6 nm dominate. The proportion of loops with size of 1–2 nm is decreased sharply from 27.5% at 573 K to only 1.5% at 1073 K. In W-5Re alloy, the variation trend of loop size distributions is similar to that of pure W alloy at 773 and 873 K. The loops with size of 1–2 nm dominate in the W-5Re alloy at 773 and 873 K, which accounts for approximately 35% of the total loops. However, at 1073 K, the proportion of loops with 1–2 nm in size drops to approximately 20%, and the maximum proportion of loops is about 24% for the ones with 4–5 nm in size. At 1073 K, the number of loops is much lower than that at 873 K, suggesting that fewer loops nucleate at this temperature but more loop growth occurs. The loop size distributions in W-5Ta alloy slightly change under different irradiation temperatures. The dominant loop size is 1–2 nm, and the proportion of these loops is decreased from 42% to 30% with increasing the irradiation temperatures. The proportion of loops with size of 4–5 nm is increased from 6% to 11% with increasing the irradiation temperature from 873 K to 1073 K. The loops with 8 nm in size can only be observed at 1073 K. Additionally, Ta has a larger effect than Re on the restriction of loop growth during irradiation^[47].

4 SiC Composites

The application of SiC fiber-reinforced SiC ceramic composites (SiC/SiC) in nuclear reactors becomes a research hotspot, and its initial application is in the high-temperature

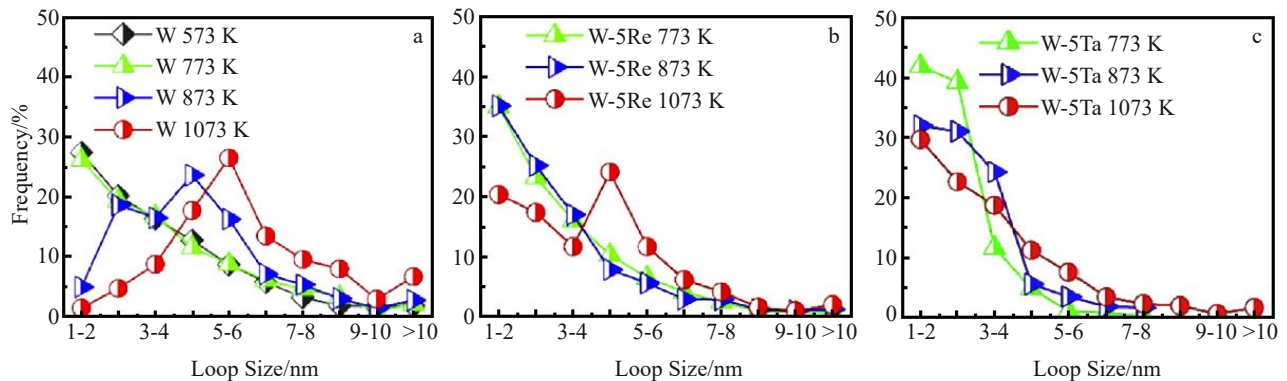


Fig.11 Loop size distributions along <001> axis in pure W (a), W-5Re (b), and W-5Ta (c) alloys after irradiation to 1.0 dpa^[47]

gas-cooled reactors. Although the fracture strength (measured by proportional ultimate stress) decreases after irradiation at 300 °C, it barely changes after irradiation at 500 and 800 °C. When the pure SiC and SiC/SiC composites are treated by irradiation at 500–1000 °C with dose of 70 dpa, the high strength, good dimensional stability, and even the excellent compatibility in liquid Pb-Li at 1100 °C of SiC composites can be maintained.

Han et al^[48] studied the irradiation resistance of SiC/SiC composites by Au ion irradiations at 10 MeV and 350 °C with surface doses of 1–50 dpa. The irradiation-induced axial and radial shrinkage of SiC-fibers was discussed, as shown in Fig. 12. After irradiation to 50 dpa, the net fiber shrinkage reaches 2.8%±0.3%. The primary cause of SiC-fiber shrinkage in SiC/SiC composites is the loss of pre-existing carbon packets, which account for 2%–3% fiber in un-irradiated composite. The volume of carbon packet is decreased with increasing the dose, and the carbon packet is basically completely lost after irradiation to 50 dpa. In addition, the irradiation-induced swelling of 1%±0.5% can be observed in the matrix after irradiation to 50 dpa. In this case, the multilayer pyrolytic-carbon (PyC) interface in the composite has high irradiation resistance, thereby maintaining its morphology and graphitic nature, and presenting no signs of amorphization. Additionally, the Raman spectroscopy results reveal that the saturation state of a TEM-invisible disorder for both the ultra-fine grains of fiber and the larger SiC-matrix grains after irradiation to 1 dpa. However, the formation of TEM-visible defects, such as dislocation loops, can only be detected in the larger matrix grains, thereby revealing a potential role of grain size on defect accumulation in SiC

composites.

The irradiation resistance of SiC/SiC composites is mainly determined by the purity and crystallinity of the materials. The lower the material purity and crystallinity, the more the structural defects after irradiation, and the worse the irradiance resistance of material. Conversely, the higher the purity and crystallinity, the better the structural stability, and the better the properties under irradiation environment.

5 HEAs

HEAs usually have equal atomic ratios of the principal elements with face-centered cubic (fcc) single phase, bcc single phase, or fcc+bcc poly-phase^[49]. Compared with the traditional alloys, HEAs have better high-temperature properties, excellent corrosion resistance, and fine ion irradiance resistance^[50]. The general element composition of HEAs can be simply divided into two categories: the ones with 3D-transition group metals (Co, Cr, Cu, Fe, Mn, Ni, Ti, V) as the main constituent elements, and the ones with refractory metals (W, Mo, Nb, Ti, Ta, Zr, Cr, Hf) as the main constituent elements (refractory HEAs)^[51]. Although the superior HEAs can maintain good mechanical properties below 600 °C (strong work hardening effect, high yield strength), which are similar to Ni-based alloys, the mechanical properties are significantly reduced once the temperature reaches 800 °C^[52]. In order to prepare HEA with excellent high-temperature mechanical properties, El-Genk et al^[53] prepared WMoTaNb ($\rho=13.75 \text{ g/cm}^3$) and WMoTaNb-V ($\rho=12.36 \text{ g/cm}^3$) alloys with bcc single phase structure, which attract widespread attention due to their stable mechanical properties at even 1600 °C. Various alloys have been designed

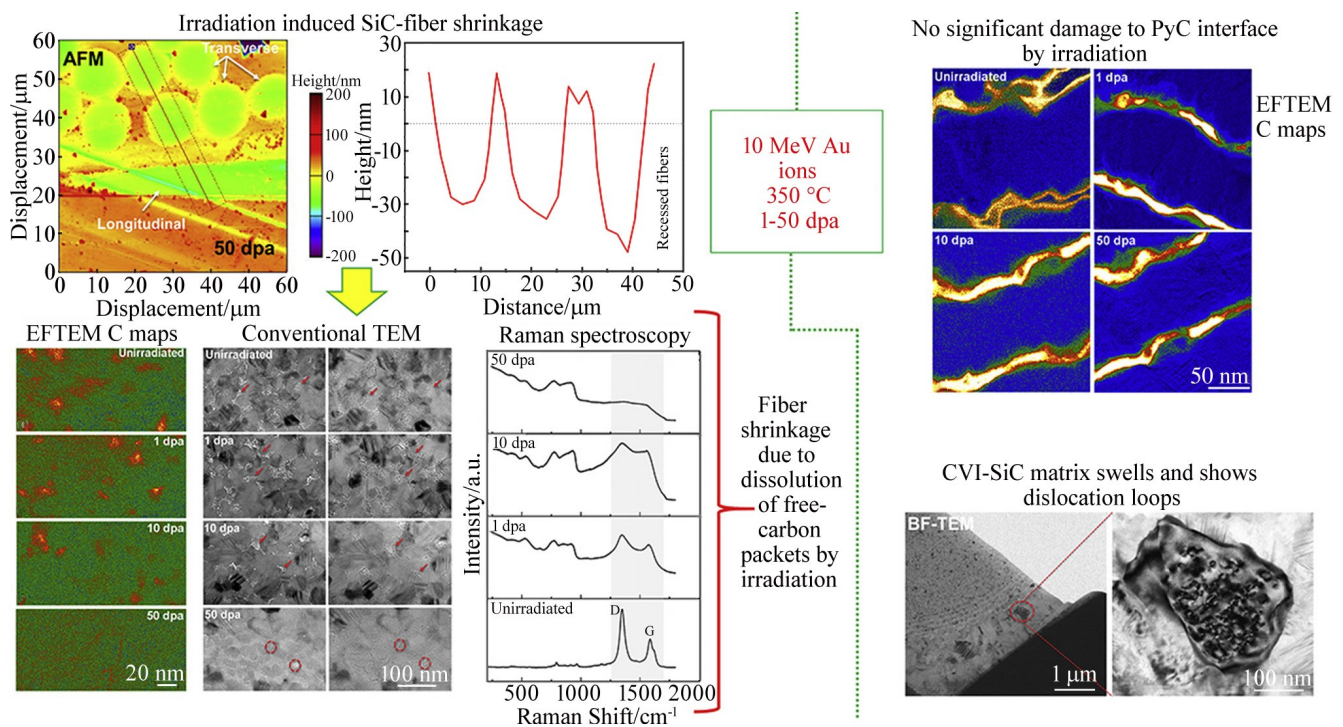


Fig. 12 Ion irradiation-induced damage in SiC/SiC composites under conditions^[48]

to improve their high-temperature mechanical properties, and the considered elements gradually change to the fourth subgroup (Ti, Zr, Hf), the fifth subgroup (V, Nb, Ta), the sixth subgroup (Cr, Mo, W), and non-refractory (Al, Si, Co, Ni) elements^[54].

To evaluate the potential of HEAs for nuclear applications, the properties of $\text{Al}_{0.3}\text{CoCrFeNi}$ and CoCrFeMnNi HEAs were compared with those of conventional 316H stainless steel after irradiation to 1 dpa with 1 MeV krypton ions at 500 °C^[55]. After irradiation, the ordered L1_2 nanoparticles with high density can be observed in $\text{Al}_{0.3}\text{CoCrFeNi}$ HEA. However, no phase transformation occurs in CoCrFeMnNi HEA and 316H stainless steel. As shown in Fig. 13^[55] and Fig. 14^[55], small defect clusters and dislocation loops can be observed in all three materials after irradiation. No voids can be observed, which may be due to the insufficient vacancy mobility and the relatively low irradiation dose. Since the thin foil specimens have wedge shape, the size and density of defects can be directly affected by the TEM observation. The areal density of defect clusters in the 2D TEM version is proportional to the foil thickness, but it is not identical to that in the 3D observation version.

Fig. 13 shows the dark-field TEM images of $\text{Al}_{0.3}\text{CoCrFeNi}$ HEA, CoCrFeMnNi HEA, and 316H stainless steel after irradiation to 1 dpa with 1 MeV krypton ions at 500 °C. The thickness of foil specimens was 80 nm. In this case, only small defect clusters can be observed. For the $\text{Al}_{0.3}\text{CoCrFeNi}$ and CoCrFeMnNi HEAs, the high portion of defect clusters can be recognized as stacking fault tetrahedra. The stacking fault tetrahedra in $\text{Al}_{0.3}\text{CoCrFeNi}$ HEA is slightly larger with better configuration, compared with that in CoCrFeMnNi HEA. For 316H stainless steel, only a few defect clusters are stacking fault tetrahedra, as indicated by the red arrows in Fig. 13c. Other features do not have a well-defined shape and are considered as dislocation loops. Moiré fringes on surface oxides can be observed in CoCrFeMnNi HEA, which are more obvious than those in the $\text{Al}_{0.3}\text{CoCrFeNi}$ HEA and 316H stainless steel.

When the foil thickness is more than 100 nm, large dislocation loops of 40 nm in size appear uniformly, as shown

in Fig. 14^[55]. The loop size is larger than the black-spot defect clusters in the thinner regions. The areal density of dislocation loops is increased with increasing the foil thickness. For $\text{Al}_{0.3}\text{CoCrFeNi}$ HEA, a large number of small defect clusters are still visible in the thick region, resulting in a bimodal size distribution of defect clusters. For the CoCrFeMnNi HEA and 316H stainless steel, the bimodal distribution is not obvious. When the foil thickness is 250 nm, no dislocation networks can be observed. No quantitative measurement is conducted on the stacking fault tetrahedra and small defect clusters in the thick regions, because small defect clusters with size < 2 nm are difficult to detect in the foils with thickness > 40 nm.

Refractory HEAs attract much attention due to their excellent high-temperature mechanical properties. Since the reactor core material serve under harsh conditions, including high temperature, strong corrosion, and high-dose irradiation, the WMoTaNb refractory HEA with excellent high-temperature strength has great potential in the irradiation field^[56]. The energy for WMoTaNb and FeCoCrNi HEAs during He irradiation is similar^[57]. Numerous studies prove that FeCoCrNi HEAs have excellent irradiation resistance^[58], so WMoTaNb refractory HEAs are expected to have excellent ionic irradiation properties.

The W-based refractory HEA with bcc structure and outstanding radiation resistance was designed by Wesemann et al.^[10]. The thin films have bimodal grain size distribution in the nanocrystalline and ultrafine grains. A lamellar structure of 4 nm in size can be observed by APT, as shown in Fig. 15^[10]. Some black spots appear after thermal annealing at elevated temperatures in W-based refractory HEA. It is revealed that the black spots with secondary phase particles are rich in Cr and V elements. As shown in Fig. 15, no sign of irradiation-created dislocation loops, even after dose to 8 dpa, can be observed. Furthermore, the hardness of 14 GPa is obtained for the as-deposited specimens with almost negligible irradiation hardening effect. The formation of Cr- and V-rich secondary phase particles can be predicted. The point defects with equal-mobilities are the origin of the exceptional radiation tolerance.

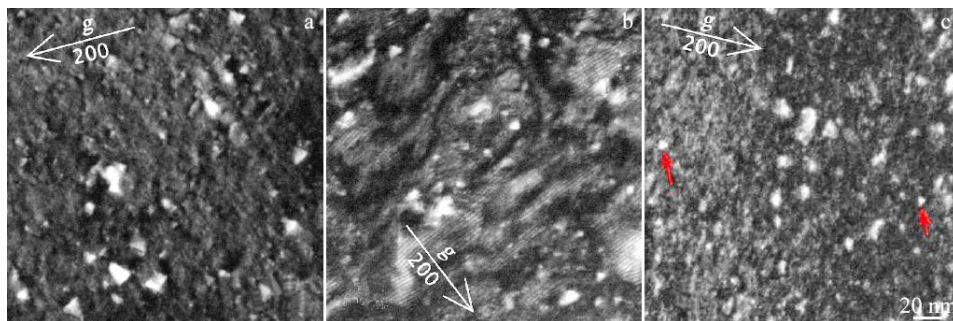


Fig. 13 Weak-beam dark-field TEM images of $\text{Al}_{0.3}\text{CoCrFeNi}$ HEA (a), CoCrFeMnNi HEA (b), and 316H stainless steel (c) after irradiation to 1 dpa with 1 MeV krypton ions at 500 °C (the thickness of foil specimen is 80 nm; the diffraction condition is $g=[200]$ at $\langle 011 \rangle$ zone axis; the red arrows indicate stacking fault tetrahedra in 316H stainless steel; the Moiré fringes in CoCrFeMnNi HEA are oxides on the foil surface)^[55]

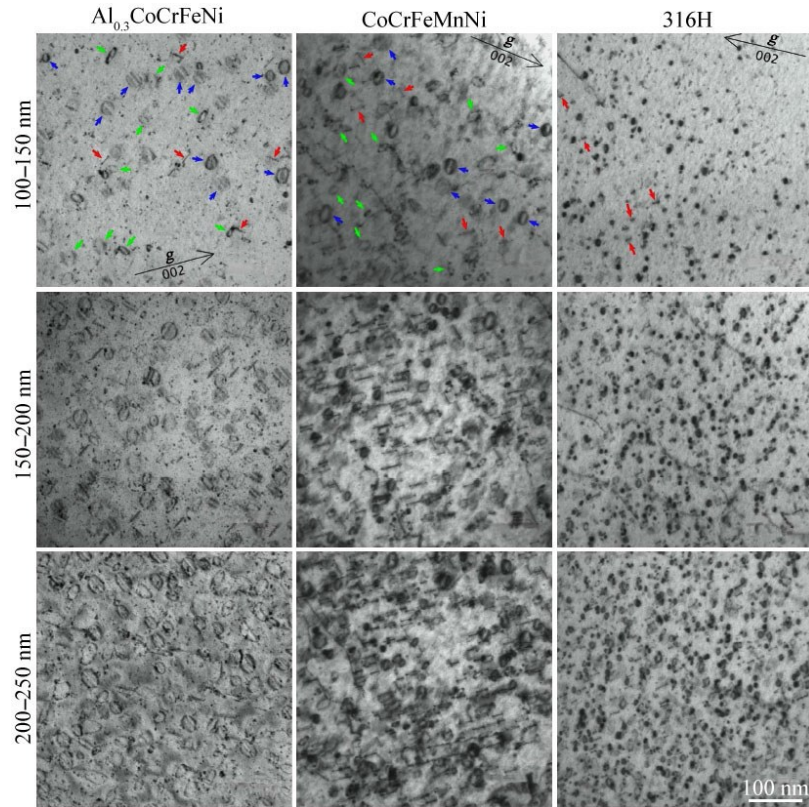


Fig.14 BF TEM images near $\langle 110 \rangle$ zone axis with $g=[200]$ of $Al_{0.3}CoCrFeNi$ HEA, $CoCrFeMnNi$ HEA, and 316H stainless steel with different thicknesses after irradiation to 1 dpa with 1 MeV krypton ions at $500^\circ C^{[55]}$

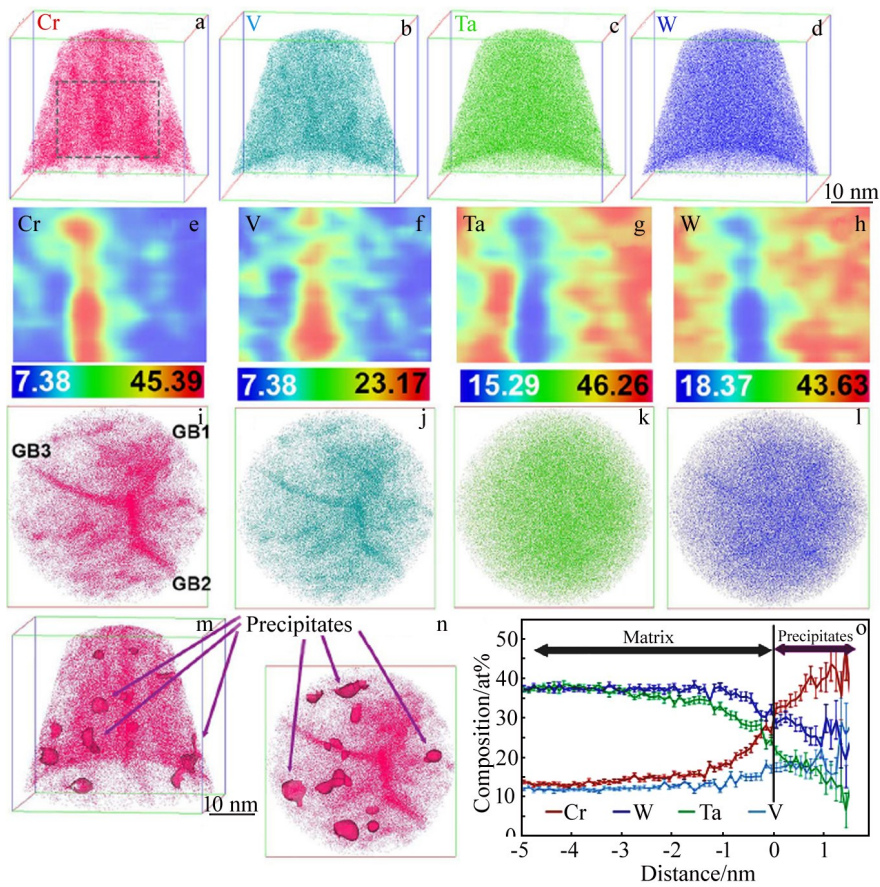


Fig.15 APT analysis results of W-based refractory HEA after Cu^+ irradiation to 8 dpa at 3 MeV and $1050 K^{[10]}$

6 Conclusions

1) Stainless steels with relatively low cost have good irradiation-resistance at low temperature. Thus, a series of modified cast stainless steels based on the standard 316L stainless steel have been developed and characterized. These steels are modified by nitrogen, manganese, and copper, exhibiting smaller elemental inhomogeneity and better structural stability during irradiation. As a potential steel system, the reduced activation ferritic/martensitic (RAFM) steel has better performance than the austenitic stainless steel does as structural materials in the application of fusion reactor. W, Ta, and V elements replace the Mo, Ni, and Nb elements in RAFM to reduce the activation and to obtain the relatively smaller deuterium retention.

2) Although Ni-based superalloys and high entropy alloys possess good irradiation-resistance, the phase transformation leads to the unstable structure and inferior mechanical properties, which restricts their application at high temperatures. After the solid solution, Mo, W, Nb, and their alloys with high melting points present excellent irradiation resistance. However, Mo and W are fragile at room temperature. The addition of Re element can improve the ductility of Mo and W, but degrade their irradiation resistance by hardening effect and the secondary phase precipitation.

3) SiC/SiC composite materials have excellent properties and low activation characteristics. However, the practical application of the SiC/SiC composite materials is restricted to a certain extent by the seal preservation problem (minimize the permeability of gas), production of materials, industrial feasibility (welding process), and manufacturing cost.

References

- Byun T S, Hashimoto N, Farrell K. *Journal of Nuclear Materials*[J], 2006, 351(1–3): 303
- Hashimoto N, Zinkle S J, Rowcliffe A F et al. *Journal of Nuclear Materials*[J], 2000, 283–287(1): 528
- Busby J, Hoelzer D, Kenik E et al. *International Conference on Fusion Reactor Materials*[C]. Nice: International Atomic Energy Agency, 2007
- Tan L, Hoelzer D T, Busby J T et al. *Journal of Nuclear Materials*[J], 2012, 422(1–3): 45
- Kenik E A, Busby J T, Gussev M N et al. *Journal of Nuclear Materials*[J], 2017, 483: 35
- Huang Qunying, Li Chunjing, Li Yanfang et al. *Chinese Journal of Nuclear Science and Engineering*[J], 2007, 27(1): 41 (in Chinese)
- Li Xinggang, Yan Qingzhi, Ge Changchun. *Journal of Iron and Steel Research*[J], 2009, 21(6): 6 (in Chinese)
- Lindau R, Moslang A, Rieth M et al. *Fusion Engineering and Design*[J], 2005, 75: 989
- Wang P H, Chen J M, Fu H Y et al. *Journal of Nuclear Materials*[J], 2013, 442(1–3): S9
- Wesemann I, Hoffmann A, Mrotzek T et al. *International Journal of Refractory Metals and Hard Materials*[J], 2010, 28(6): 709
- Huang Q, Li C, Li Y et al. *Journal of Nuclear Materials*[J], 2007, 367–370(A): 142
- Xiong X S, Yang F, Zou X R et al. *Journal of Nuclear Materials*[J], 2012, 430(1–3): 114
- Hu X X, Tan L Z, Wang K et al. *Journal of Nuclear Materials*[J], 2019, 516: 144
- David A, Maxim N, Campbell C et al. *Acta Materialia*[J], 2022, 231: 117 889
- Byun T S, Farrell K. *Journal of Nuclear Materials*[J], 2003, 318: 292
- Li J Y, Marquis E A. *Journal of Nuclear Materials*[J], 2021, 553: 153 040
- Leonard K J. *Comprehensive Nuclear Materials*[J], 2012, 4: 181
- Li J T, Beyerlein I J, Han W Z. *Acta Materialia*[J], 2022, 226: 117 656
- Souza F I R, Dutta A, Junior D R A et al. *Acta Materialia*[J], 2020, 197: 123
- Bisson E E, Anderson W J. *Advanced Bearing Technology*[M]. Ohio: National Aeronautics and Space Administration, 1964
- Schneibel J H, Brady M P, Kruzic J J et al. *Zeitschrift für Metallkunde*[J], 2022, 96(6): 632
- Li Y P, Ran G, Guo Y J et al. *Acta Materialia*[J], 2020, 201: 462
- Mahajan S, Eyre B L. *Acta Materialia*[J], 2017, 122: 259
- Busby J T, Leonard K J, Zinkle S J J. *Journal of Nuclear Materials*[J], 2007, 366(3): 388
- Hasegawa A, Kazukiyo U, Manabu S et al. *Journal of Nuclear Materials*[J], 1998, 258: 902
- Johnson P K. *14th International Plansee Seminar*[C]. Reutte: International Journal of Powder Metallurgy, 1997(8): 72
- Nordlund K, J-Zinkle S, E-Sand A. *Journal of Nuclear Materials*[J], 2018, 512: 450
- Nemoto Y, Hasegawa A, Satou M et al. *Journal of Nuclear Materials*[J], 2004, 324(1): 62
- Krajnikov A V, Morito F, Danylenko M I. *Journal of Nuclear Materials*[J], 2014, 444(1–3): 404
- Fabritsiev S A, Pokrovsky A S. *Journal of Nuclear Materials*[J], 1998, 252(3): 216
- Qiu X, Pang H, Ran G et al. *Journal of Nuclear Materials*[J], 2022, 559: 153 443
- Katoh Y, Snead L L, Garrison L M et al. *Journal of Nuclear Materials*[J], 2019, 520: 193
- Fan C C, Li C Y, Parish C M. *Acta Materialia*[J], 2021, 203: 116 420
- Greaves G, Hinks J A, Donnelly S E. *Journal of Nuclear Materials*[J], 2019, 514: 123
- Ferroni F, Yi X O, Arakawa K et al. *Acta Materialia*[J], 2015, 90: 380
- Yi X O, Jenkins M L, Kirk M A et al. *Acta Materialia*[J], 2016, 112: 105

- 37 Yang Q, Fan H Y, Ni W Y et al. *Acta Materialia*[J], 2015, 92: 178
- 38 Agarwal S, Duscher G, Zhao Y et al. *Acta Materialia*[J], 2018, 161: 207
- 39 Tang Z, Gao M C, Diao H et al. *JOM*[J], 2013, 65: 1848
- 40 Li Z Z, Zhao S T, Ritchie R O et al. *Progress in Materials Science*[J], 2019, 102: 296
- 41 Senkov O N, Miracle D B, Chaput K J et al. *Journal of Materials Research*[J], 2018, 33(19): 3092
- 42 Gorsse S, Miracle D B, Senkov O N. *Acta Materialia*[J], 2017, 135: 177
- 43 Senkov O N, Wilks G B, Miracle D B et al. *Intermetallics*[J], 2010, 18(9): 1758
- 44 Senkov O N, Wilks G B, Scott J M et al. *Intermetallics*[J], 2011, 19(5): 698
- 45 Chen W Y, Kirk M A, Hashimoto N et al. *Journal of Nuclear Materials*[J], 2020, 539: 152 324
- 46 Dobbstein H, Thiele M, Gurevich E L et al. *Physics Procedia*[J], 2016, 83: 624
- 47 Han Z D, Chen N, Zhao S F et al. *Intermetallics*[J], 2017, 84: 153
- 48 Han Z D, Luan H W, Liu X et al. *Materials Science and Engineering A*[J], 2018, 712: 380
- 49 El-Atwani O, Li N, Li M et al. *Science Advances*[J], 2019, 5(3): eaav2002
- 50 Was G S, Petti D, Ukai S et al. *Journal of Nuclear Materials*[J], 2019, 527: 151 837
- 51 Hosemann P, Frazer D, Fratoni M et al. *Scripta Materials*[J], 2018, 143: 181
- 52 Zinkle S J, Was G S. *Acta Materials*[J], 2013, 61(3): 735
- 53 El-Genk M S, Tournier J M. *Journal of Nuclear Materials*[J], 2005, 340(1): 93
- 54 Lee H B, Chen J J, Meng S et al. *Journal of Nuclear Materials*[J], 2021, 556: 153 193
- 55 Wu Z F, Xu L D, Chen H Q et al. *Journal of Nuclear Materials*[J], 2022, 559: 153 418
- 56 Katayama K, Matsumoto T, Ipponsugi A et al. *Journal of Nuclear Materials*[J], 2022, 565: 153 723
- 57 Liu J Z, Huang H F, Gao J et al. *Journal of Nuclear Materials*[J], 2019, 517: 328
- 58 Dutta A, Sarkar A, Mukherjee P et al. *Journal of Nuclear Materials*[J], 2021, 557: 153 221

抗辐照材料研究进展

徐海龙^{1,2}, 黄 丽², 张 文², 高选乔², 杨毅超^{2,3}, 单智伟¹, 李建峰²

(1. 西安交通大学 材料科学与工程学院, 陕西 西安 710049)

(2. 西北有色金属研究院, 陕西 西安 710016)

(3. 西北工业大学, 陕西 西安 710072)

摘要: 用于核反应堆的新候选材料研发是一项重要任务。由于反应堆环境恶劣, 堆芯材料在高温下应具有良好的综合性能, 如良好的强度、延展性、耐腐蚀性能和耐辐照性能等。此外, 还应考虑低中子吸收横截面和中子活化。典型的空间核反应堆核心材料的选择主要由工作温度决定。随着反应堆设计工作温度的升高, 一般以316不锈钢、镍基高温合金、氧化物分散强化(ODS)钢、铌合金、难熔金属和SiC陶瓷的顺序来选择设计堆芯材料。此外, 高熵合金已经引起核领域的广泛关注。本文综述了以上不同材料体系在辐照过程中的力学性能演变, 为进一步提升抗辐照性能提供研究指导。

关键词: 抗辐照; 力学性能; 核工程

作者简介: 徐海龙, 男, 1984年生, 硕士, 高级工程师, 西北有色金属研究院, 陕西 西安 710016, 电话: 029-86231105, E-mail: 187298751@qq.com